Wide Bandgap Mixed-halide 3D Perovskites: Electronic Structure and Halide Segregation Investigation

Siyuan Zhang,[†^*] *Ming-Chun Tang,*[†‖§] *Nhan V. Nguyen,*[†] *Thomas D. Anthopoulos,*[‖*] *Christina A. Hacker*[†*]

[†]Physical Measurement Laboratory, National Institute of Standards and Technology (NIST) Gaithersburg, MD 20899, USA

[‖]King Abdullah University of Science and Technology (KAUST), KAUST Solar Center (KSC), and Physical Science and Engineering Division (PSE), Thuwal, 23955-6900, Saudi Arabia.

[§]Institute for Research in Electronics and Applied Physics & Maryland NanoCenter, University of Maryland, College Park, MD 20742, USA

[^] Theiss Research, La Jolla, CA 92037, USA

S. Z. and M-C. T. contributed equally to this work.

KEYWORDS: perovskite, electronic structures, photoemission spectroscopy, depth profile, microstructure, phase segregation

ABSTRACT

Mixed-halide organolead perovskites ($MAPbX_3$) are of great interest for both single junction and tandem solar cells because of their wide bandgap. In this study, we investigate the family of mixed iodide/bromide (I/Br) and bromide/chloride (Br/Cl) perovskites, revealing the strong influence of halide substitution on electronic properties, morphology, film composition, and phase segregation.

A qualitative blue-shift with the I →Br →Cl series was observed with the resulting optical absorption ranging from 420 nm to 800 nm covering nearly the entire visible region. The ionization potential increases from ≈6.0 eV to ≈7.0 eV as the halide composition changes from I to Br. However, with Cl components, the valence band position shows little variation, while the conduction band edge shifts upward with increasing Cl composition. By collecting XPS spectra as a function of sputtering depth, we observed halide segregationboth I/Br and Br/Cl mixed-halide perovskite films, where the large halide ion (I in I/Br mix or Br in Br/Cl mix) is preferrentially found on the surface of the film and the smaller halide ion (Br in I/Br mix or Cl in Br/Cl mix) accumulates at the bottom of the film. These differences in the band structure, electronic properties, morphology, and film composition impacted the device performance: a decreased short-circuit current density and increased open-circuit voltage was observed with the I →Br →Cl series. This study highlights the role of halides in the band structure and phase segregation in mixed-halide perovskite solar cells and provides a foundational framework for future optoelectronic applications of these materials.

INTRODUCTION

Organic-inorganic hybrid lead-based halide perovskites have been attracting an ever-growing interest, and their certified solar cell power conversion efficiency (PCE) has exceeded 25 %.[1] The versatile synthesis of this class of materials offers a wide range of band gaps, optical and electrical tunability, which makes these materials very attractive for a variety of applications beyond light-harvesting devices, to include light-emitting diodes (LEDs),[2] lasers,[3] photodetectors,[4] photocatalysts,[5] transistors,[6] and memory devices.[7] Wide bandgap mixed-halide perovskites are promising candidates to boost the PCE of conventional silicon photovoltaics (PV) toward >30 % in tandem junction architectures. By stacking complementary wide bandgap and narrow bandgap

absorbers, the thermalization losses can be largely reduced and the device can exceed the Shockley–Queisser limit of a conventional single-junction solar cell.[8-9] For example, in order to match the bandgap of a Si cell (≈1.1 eV) in tandem devices, a bandgap of ≈ 1.75 eV for the top cell layer is required.[10]

With the formula of ABX_3, perovskite-based PVs consist of the organic cation (A) including methylammonium (MA^+), formamidinium (FA^+), dimethylammonium (DMA^+), and/or cesium (Cs^+), B is lead (Pb^{2+}) or tin (Sn^{2+}), and halide ions (X) includes chloride (Cl), bromide (Br), iodide (I), or the mixture.[11-12] The PCEs of single junction perovskite cells have achieved very high efficiency,[1, 13-16] while the bandgaps of these films are around ≈1.55 eV, which is too small to match the bandgap of Si solar cells in tandem devices. To provide wider bandgap perovskites, one of the strategies is to develop mixed-halide hybrid perovskites.[17-19] By integrating wide-bandgap perovskite top cells with silicon bottom cells, PCEs over 28% have been achieved in two-terminal monolithic tandem solar cells.[20]

However, as the bandgaps reach the optimum 1.7 eV to 1.8 eV range, fundamental issues, such as photoinstability and photoinduced phase segregation, have been discovered. It has been reported that the increased Br fraction of the X halide ion, in $MAPb[I_{(1-x)}Br_x]_3$ under illumination, can lead to the formation of light-induced halide segregation and impacts the photostability of mixed-halide perovskites. The iodide-rich domains with smaller bandgap increase the sub-gap absorption, leading to a redshift of the photoluminescence (PL), and reduces the open-circuit voltage (V_{oc}).[21-22] Moreover, Chen *et al.* reported a two-photon confocal microscopy investigation of dynamic photoinduced phase segregation and phase recovery in mixed-halide $MAPbBr_xI_{3-x}$ perovskite single crystals under dark conditions, indicating the Br-phase is dispersed in the interior of the microplatelets while I substitution tends to occur at the crystal edges.[23] The photoinduced phase

segregation can be reduced through the substitution of MA or FA to Cs or DMA while limiting the Br fraction.[24-25] The ability to control or prevent photoinduced phase segregation in perovskites is crucial to realizing stable and tunable mixed-halide optoelectronic devices. Phase segregation information can be extracted from the optical or electrical properties using techniques such as absorption and photoluminescence spectroscopy, external quantum efficiency (EQE), transient absorption spectroscopy, and photovoltaic performance.[20, 25-26] However, these techniques characterize the bulk electrical or optical properties of the film and cannot give information about the spatial distribution. In this study, we use X-ray photoemission spectroscopy depth profiling to map the elemental distribution in multi-halide perovskites.

In this study, we systematically investigate the role of halide substitution in mixed-halide $MAPbX_3$ perovskites on their morphology, electronic structure, chemical compositions, and so on, to provide insight into the properties of pure and mixed-halide $MAPbX_3$ perovskites in relation to their potential application in photovoltaics. Correlating investigations between crystal structure, optical properties, and phases are performed for different halide-substituted $MAPbX_3$, by scanning electron microscopy (SEM), UV−vis absorption spectroscopy, X-ray diffraction (XRD), and ultra-violet and X-ray photoemission spectroscopy (UPS and XPS). The formation of pinhole-free high-quality mixed-halide perovskite films was confirmed by SEM and XRD. The band structure can be effectively tuned by precise control over the halide composition in $MAPbX_3$ films. Halide inhomogeneity was observed in mixed-halide perovskite films, as evidenced by the XPS depth profile. This fundamental information about the $MAPbX_3$ perovskite films can be expected to guide the synthesis of new perovskite films and the design of optimal cell structures.

RESULTS AND DISCUSSION

To study the effects of halide substitution on the properties of $MAPbX_3$ perovskite films, the precursor solutions were prepared at the desired reaction ratios and then spin-coated on the substrate using the one-step deposition protocol with chlorobenzene (CB) as antisolvent, followed by thermal annealing treatment. (see *Experimental Details*). The resulting films include $MAPbI_3$, $MAPbI_{1.5}Br_{1.5}$, $MAPbBr_3$, $MAPbBr_{1.5}Cl_{1.5}$, and $MAPbCl_3$. The morphology of hybrid perovskite thin films can be controlled through the solvent engineering approach via dripping antisolvent. This method has been widely used in a one-step classic $MAPbI_3$ deposition. The antisolvent dripping at an optimized timing during spin coating the perovskite ink is critical for uniform films. [11, 27]

Morphology and Crystal Structures. First, we investigate the morphology with SEM from small bandgap $MAPbI_3$ to wider bandgap hybrid halide perovskites with mixing Br and Cl halides. Appropriate use of CB dripping has been shown to quickly extract the precursor DMSO solvent and increase nucleation and crystal growth to obtain high quality and fully covered perovskite morphology on the substrates with fewer pinholes.[28-29] **Figure 1**(a-e) shows the representative scanning electron microscopy (SEM) images of pure and mixed-halide $MAPbX_3$ perovskite films. The SEM images show that all five films have good surface coverage and film uniformity on the substrates with different grain sizes and irregular grain boundaries. As shown in Figure 1d and e, the incorporation of chlorine leads to the formation of a few pinholes. The origin of these pinholes is likely due to the nucleation and growth behavior of intermediate phases other than the perovskite phase which can have different unit cell sizes that lead to cracking upon transformation into the perovskite phase.

To understand the impact of halide modification on the microstructure of the polycrystalline hybrid perovskite layers, XRD was performed on these films. **Figure 1f** shows the XRD patterns of the

tetragonal phase $MAPbI_3$ perovskite films. The peaks at 14.1°, 28.4°, and 31.7° were attributed to the (110), (220), and (310) diffraction planes of the $MAPbI_3$ perovskite polycrystalline structures, respectively. Notably, there is only a (110) diffraction peak at 14.1° from the $MAPbI_3$ perovskite phase without the non-perovskite PbI_2 diffraction peak featured at 12.6°, indicating complete $MAPbI_3$ perovskite conversion. The cubic structure of the halide substituted perovskite thin films are also verified via *ex-situ* XRD measurements. The peak of (100) diffraction plane shifts from 14.5 ($MAPbI_{1.5}Br_{1.5}$, Figure 1g), 15.1 ($MAPbBr_3$, Figure 1h), 15.4 ($MAPbBr_{1.5}Cl_{1.5}$, Figure 1i), to 15.7 ($MAPbCl_3$, Figure 1j) degrees, indicating a decrease in lattice spacing in these cubic perovskites which is caused by the decreasing size of the halide ions.[30-31] The structural changes of the unit cells from tetragonal ($MAPbI_3$) into cubic (other pure and mixed-halide perovskite films) alters the lattice constant. It has been reported that the cubic phase is usually more stable than the tetragonal phase.[32-33] To conclude, the polycrystalline structure of perovskite thin films can be effectively altered through the simple one-step spin coating of perovskite precursor solutions with different halide ratios.

Band structure and Energetics. In order to map the band structure as a function of halide content, we investigate the energetics of the occupied states and bandgaps by using ultraviolet photoemission spectroscopy (UPS) and UV-vis absorption spectroscopy, respectively. UV-Vis absorption spectra and photographs of perovskite films were measured and are shown in Figure 2a. As shown in the insert, the film color changes from dark black to orange, then to semi-transparent yellow and becoming transparent with increasing Br or Cl content in the perovskite structure. The gradual shifts in the absorption edge from 1.6 eV to 3.1 eV were observed as I is replaced by Br and then by Cl. This is caused by the decreased length of the Pb-X bonds within the network of corner-sharing octahedra as the ion size changes ($Pb\text{-}X_6$, X = I, Br, Cl).[34-35] An

increased excitonic pre-peak related to the increasing exciton binding energy was also observed as the halide changed from I to Br and Cl. These observations are consistent with previously reported literature.[34] As the bandgap increases, the hybrid perovskite thin films can act as a light-absorbing layer and convert sunlight to electricity from high energy visible to ultraviolet sunlight radiation.

Figure 2c shows the high binding energy cutoff region (i.e., secondary electron edge, SEE) and the low binding energy part of the UPS spectra as a function of the halide substitution, in which all energies are referenced to a common Fermi Level (E_f = 0 eV). The work function ϕ was determined from the high binding energy cutoff region (i.e., secondary electron edge, SEE), given by the difference between the energy of the UV photons (21.21 eV for the He I radiation used here) and the binding energy of the SEE ($E_f = E_{He(I)} - E_{SEE}$). The ionization energy (IE) can be extracted from the energy difference of valence band maximum (VBM) relative to the vacuum level (E_{VAC}). The detailed evolution of UPS spectra and the standard deviation from averaging the results obtained with different samples and spots were summarized in Supporting Information (Table S1). The corresponding energy diagrams of the perovskite films are summarized in Figure 2b. It is noted that the Fermi level is close to the conduction band minimum (CBM), indicating that all of these perovskite films function as n-type semiconductors. Both n- and p-type transport have been reported for perovskite field-effect transistors.[36-38] Self-doping effects have been observed in perovskite films where the charge transport type can be controlled by changing the precursor ratios and post-treatment condition.[39-40] In our work, all of the films were prepared with 1:1 methylammonium halide (MAX) to lead halide (PbX_2) precursor ratios and annealed at 100 °C for 10 min, both of which will lead to the n-type behavior of perovskite films. The position of the CBM (E_{CBM}) is calculated from the position of VBM and the bandgap value. $MAPbI_3$ yielded the smallest ϕ of 4.58 eV and IE of 6.01 eV. Full substitution of I to Br and Cl increase the ϕ to 5.14

eV and 4.86 eV, and IE to 6.99 eV and 6.95 eV, for $MAPbBr_3$ and $MAPbCl_3$ films, respectively. For the mixed-halide films, $MAPbI_{1.5}Br_{1.5}$ and $MAPbBr_{1.5}Cl_{1.5}$, the position of ϕ and IE lie in between the pure halide films. It worth noting that the IE increases from ≈6.0 eV to ≈7.0 eV as the I substituted by Br, while little variation was observed when Br is substituted by Cl and a monotonic trend is found for the conduction band edge. These numbers are slightly different from the literature reported value,[34, 41] which may be attributed to variations in film processing and post-treatment conditions. The UPS is mostly sensitive to the top 2 – 3 nm surface region due to the lower kinetic energy of the emitted photoelectrons (21.2 eV) and surface contaminants may impact the measured UPS spectra during the film preparation and transfer.

Composition Analysis. Figure 3 shows the evolution of XPS C 1s, N 1s, Pb 4f, I 3d, Br 3d, and Cl 2p spectral regions in the mixed-halide perovskite films. The elements are fitted by using Lorentzian-Gaussian peaks. The C 1s core-level spectra from all of the films contain two components: one at ≈284.5 eV, which is assigned to surface absorbed amorphous carbon, and another one at ≈285.9 eV is attributed to the C-N bond in MA^+ and FA^+ cations, according to the literature.[42-43] The presence of MA cations is also confirmed by the N 1s peak at 401.9 eV. The Pb 4f spectra from the $MAPbI_3$ film shows a sharp doublet located at 138.0 eV (Pb $4f_{7/2}$) and 142.9 eV (Pb $4f_{5/2}$), respectively, which are assigned to the Pb^{2+} metal ion. The peak positions of I $3d_{5/2}$, Br $3d_{5/2}$, and Cl 2p located at 618.8 eV, 67.8 eV, and 196.2 eV are also consistent with the literature reports.[42] Except for the C 1s, all of the other elements' core levels consist of only one oxidation state indicating homogenous films with these elements existing as only one chemical species within the perovskite films. The XPS core-level spectra of these elements in mixed-halide perovskite films were summarized in Figure S3.

To further analyze the distribution of components throughout the film, we measured the depth profile of the five perovskite films by XPS in the dark within a high vacuum chamber. During the measurement, a 1 keV Ar ion gun was used to etch the sample and spectra were acquired layer by layer until the observation of an abrupt decrease in the Pb 4f signal with an increase in the O 1s and Sn 3d signals from the substrate. The sputtering rate used here was controlled to ≈ 0.2 nm s^{-1} to minimize sputtering-induced physical damage and the sputtering time was converted to depth assuming a constant etch rate (refer to *Experimental Details*). It has been reported that sputtering beam-induced artifacts within perovskites can be reasonably neglected when using fast analysis conditions during which the exposure time is limited to a few hours.[44] The film thicknesses were measured by using profilometry and ellipsometry and are reported in the Supporting Information (Figure S1 and Table S2). Figure 4 illustrates the perovskite film elemental composition as a function of depth collected with XPS by using *in situ* Ar^+ sputtering. The depth profiles of $MAPbI_{1.5}Br_{1.5}$ and $MAPbBr_{1.5}Cl_{1.5}$ are shown as an example. Surface absorbed amorphous carbon is evident on the top surface, and no other surface contamination is observed. The C 1s and O 1s fractions are reduced mainly after the first sputter cycle, and the Pb 4f and I 3d fraction from the perovskite layer increase, indicating the removal of the surface absorbed carbon and oxygen. To better present the film composition, the atomic ratio of halides (I 3d and Br 3d) to lead Pb^{2+} (Pb 4f) in $MAPbI_{1.5}Br_{1.5}$ and $MAPbBr_{1.5}Cl_{1.5}$ films and summarized in Figure 4b and 4d. The I/Pb ratios in $MAPbI_{1.5}Br_{1.5}$ films decrease from ≈1.96 to ≈1.74, accompanied by increasing Br/Pb ratios from ≈0.51 to ≈1.08 as the depth increases, suggesting a bromide-poor phase was formed close to the film surface, and a bromide-rich phase was present close to the substrate. This halide segregation was also observed in $MAPbBr_{1.5}Cl_{1.5}$ film, in which the decrease of Br/Pb ratios from ≈1.90 to ≈1.63 was accompanied by increasing in the Cl/Pb ratios from ≈0.75 at the surface to

≈1.26 as the depth increases. By tracing the variation of the X:Pb ratios in mixed-halide perovskites, we found that the heavier halide ions tend to accumulate on the surface while smaller halide ions aggregate at the bottom of the film. Similar results were observed in the literature for I and Br mixed-halide perovskite films.[45-46] It has been reported that an intrinsic perovskite favors electron trapping at the top surface, which induces an electric field pointing toward the surface of the film.[47-49] To shield the trap-induced field and compensate the charge on the surface, the mobile halide ions tend to migrate away from the surface and leave the positively charged vacancies accumulated near the surface states.[50] In the mixed halide films, smaller ions (such as bromide in $MAPbI_{1.5}Br_{1.5}$, or chloride in $MAPbBr_{1.5}Cl_{1.5}$) are relatively easy to migrate, thus, leaving the heavier ions to accumulate on the surface. DFT calculation also shows that the segregation of smaller ions to the surface is energetically disfavored, while accumulations of heavier ions toward the surface leads to an overall stabilization.[51]

To investigate the impact of halide content and bandgap on perovskite solar cells, we prepared ten devices for each wide-bandgap perovskite material as a light-absorbing layer and demonstrated their device performance. Representative *J-V* curves are shown in Figure 5b. For classic and low bandgap $MAPbI_3$ solar cells, the average 16.25 ± 0.92 % of PCE is demonstrated using the same spin coating recipe. A summary of the photovoltaic parameters (Table 1) obtained from all of the perovskite solar cells contains both average and best values. While changing the halide from I to Br, then to Cl in these wide-bandgap perovskites, the average PCE ranges from 16.25 %, 10.87 %, 6.51 %, 1.08 %, and to 0.29 %, and short-circuit current density (J_{SC}) decreases due to enhancing bandgap in $MAPbI_3$, $MAPbI_{1.5}Br_{1.5}$, $MAPbBr_3$, $MAPbBr_{1.5}Cl_{1.5}$, and $MAPbCl_3$ films. The decreased J_{SC} is due to increasing bandgap leading to less sunlight absorption. The high average fill factor is stable around 68% to 77 % across all of the films. A high V_{OC} is maintained around

1.4 V for $MAPbBr_3$ and $MAPbBr_{1.5}Cl_{1.5}$ solar cells, even though $MAPbBr_{1.5}Cl_{1.5}$ has a wider bandgap, and an ultra-high V_{OC} of 1.65 V is achieved in $MAPbCl_3$ perovskite devices. The pinned V_{OC} may be attributed to the activation energy for these wide-bandgap solar cells that are much lower than the bandgap. This suggests that a high interface recombination process limits the V_{OC} and, consequently, the device performance of these wide-bandgap solar cells.[52] To overcome this problem, an investigation of alternative electron or hole transporting layers or surface modification is needed in the future.[52] It worth noting that the best perovskite device performance for $MAPbCl_3$ is PCE = 0.32 % with V_{OC} = 1.65 V. This $MAPbCl_3$ transparent perovskite thin film with the extremely high V_{OC} perovskite solar cell is also very promising in the applications of building integrated photovoltaic systems, blue and ultraviolet light-emitting diodes, and photodetectors.

CONCLUSION

In summary, we systemically investigate electronic properties, morphology, film composition, and phase segregation of a series of mixed halide $MAPbX_3$ (X = Cl, Br, and I) perovskite films. Pinhole-free high-quality $MAPbX_3$ hybrid perovskite thin films were fabricated by a simple one-step spin coating method with antisolvent dripping. Structural measurements show that I can be seamlessly substituted by Br and then by Cl, attributed to the lattice compatibility of the pure-halide composition. A full tunability of ionization potentials were observed along the I →Br →Cl series, and the light absorption of the resulting films covers the entire visible region. We also unravel the roles of halide in promoting vertical homogeneous composition distribution in perovskite films, thus preventing segregation of halides and cations. Moreover, halide inhomogeneity was observed in mixed-halide perovskite films by using XPS depth profiling. In mixed-halide perovskite films ($MAPbI_{1.5}Br_{1.5}$ and $MAPbBr_{1.5}Cl_{1.5}$), smaller halide ions tend to aggregate at the bottom, leaving a higher concentration of larger halide ions on the surface.

Although only two systems were studied, it provides insight into how halide ions might be distributed in mixed-halide perovskite films. This study provides an in-depth understanding of tunable and wide-bandgap perovskite inks, which is critical and insightful for initial design of perovskite precursor solutions to achieve better reproducibility, cost-efficient and large-scale manufacturing of lead-based hybrid perovskite solar cells in the future.

EXPERIMENTAL SECTION

Materials, lead halide precursor solutions, and deposition protocol

All the commercial instruments and materials mentioned here are identified to foster understanding. Such identification does not imply recommendation or endorsement by the National Institute of Standards and Technology, nor does it imply that the materials or equipment identified are necessarily the best available for the purpose. All the chemicals are purchased from Sigma–Aldrich unless stated otherwise. For solar cell devices, pre-patterned ITO (ITO: 15 ohm sq^{-1}—bought from Xinyan Technologies) glass substrates were used. Perovskite precursor (1M) solution was prepared by dissolving methylammonium halide (MAI, MABr, MACl), purchased from Dyesol, and each lead halide (PbI_2, $PbBr_2$, $PbCl_2$) (1:1 ratio) in dimethyl sulfoxide (DMSO) and stirred overnight at 60 °C. Thin films of perovskites were deposited by spin coating at 1000 rpm for 10 sec and 5000 rpm for 50 sec. Chlorobenzene (0.25 ml) was dropped on the spinning substrate during the second spin-coating step at 30 sec before the end of the procedure. The films were then annealed at 100 °C for 10 min.

Solar cell preparation

The solar-cell devices were fabricated using the same Cl-TiO_2 thin-film procedure on the patterned ITO-coated glass. Perovskite were prepared as above and after cooling to room temperature, the hole-transporting layer was then deposited on top of the perovskite film via spin-coating at 2000 rpm for 30 sec using chlorobenzene of a 80 mg/ml solution of 2,2′,7,7′-tetrakis-(N,N-di-methoxyphenamine) 9,9′-spirobifluorene (spiro-MeOTAD), with additives of lithium bis(trifluoromethanesulfonyl) imide and 4-tert-butylpyridine. Finally, 20 nm of gold and 80 nm of silver electrodes were deposited by thermal evaporation using an Angstrom evaporator. The current-density–voltage (*J*–*V*) curves were measured using a solar simulator (Newport, Oriel Class A, 91195A) with a source meter (Keithley 2420) at 100 mA cm^{-2} illumination (AM 1.5G) and a calibrated Si-reference cell certificated by NREL. All of the solar cells were masked during the *J*–*V* measurements to define the active area of about 0.1 cm^2.

Characterization

Scanning Electron Microscopy (SEM). A Quanta 200FEG scanning electron microscope from FEI was used to observe the morphology of the annealed perovskite films.

UV-Vis Transmission Measurements. UV–Vis absorption spectra were acquired by using a Cary 5000.

X-ray Powder Diffraction: XRD patterns via Bruker D8 advance A25 diffractometer in the Bragg–Brentano geometry equipped with a Cu tube (Cu Kα; λ = 0.15418 nm) operating at 40 kV and 40 mA using a linear position sensitive detector (opening 2.9°).

Photoemission Spectroscopy Measurements. The seven mixed-cation lead mixed-halide perovskite films were transferred into the characterization chamber for ultraviolet and X-ray photoemission spectroscopies (UPS and XPS) to determine the valence band levels and core levels.

Angle-resolved XPS was also performed to study the elemental composition and to access the metal ion distribution within the layer. UPS and XPS Spectra were acquired on the Kratos Axis Ultra^{DLD} surface analysis system, using the He-I lamp radiation (21.2 eV) and monochromatic Al Kα line, respectively.[53] The films were characterized under a base pressure < 10^{-6} Pa. All samples were in electronic equilibrium with the spectrometer via copper tape in contact with the perovskite film surface and characterized at a normal take-off angle unless stated otherwise. The Fermi level was calibrated using sputter cleaned gold film. Survey XPS scans were run at 160 eV pass energy and high-resolution scans at 20 eV pass energy. The UPS spectra were acquired at 5 eV pass energy and 0.05 eV step size with the aperture and iris set to 55 μm. From the binding energy corresponding to the SEE of the UPS spectra, we calculated the work function (φ = 21.22 eV – SEE) for each film, and from the onset of photoemission, we determine the position of the valence band maximum. XPS depth profiling was used to investigate the atomic composition of the bulk region using an Ar ion sputter gun with power 1 keV and 600 nA on a raster area of 1 mm^2. The XPS spectra were collected after 150 s sputtering time. The sputtering rate is estimated to be 0.26 nm/s, with the assumption that the film thickness is 400 nm, and it took 1500 s to fully etch through the film. The film thickness was measured by using the profilometer and ellipsometry, and the results were shown in the Supporting Information (Figure S2).

FIGURES

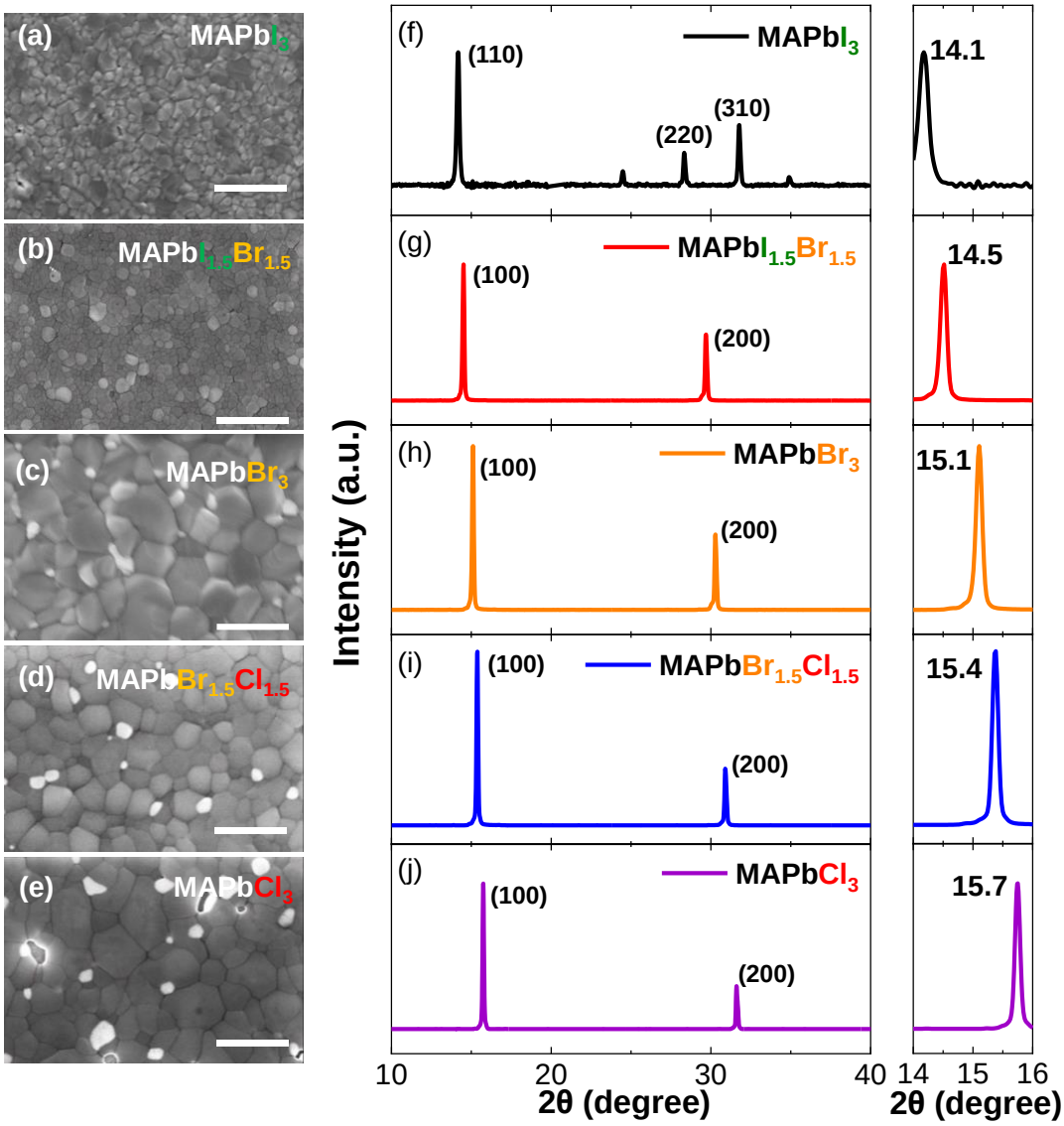

Figure 1. Surface morphologies and XRD spectra of tunable bandgap perovskite thin films: (a, f) $MAPbI_3$, (b, g) $MAPbI_{1.5}Br_{1.5}$, (c, h) $MAPbBr_3$, (d, i) $MAPbBr_{1.5}Cl_{1.5}$, and (e, j) $MAPbCl_3$ films on ITO substrates. The length of the scale bar in the SEM images is 1 μm.

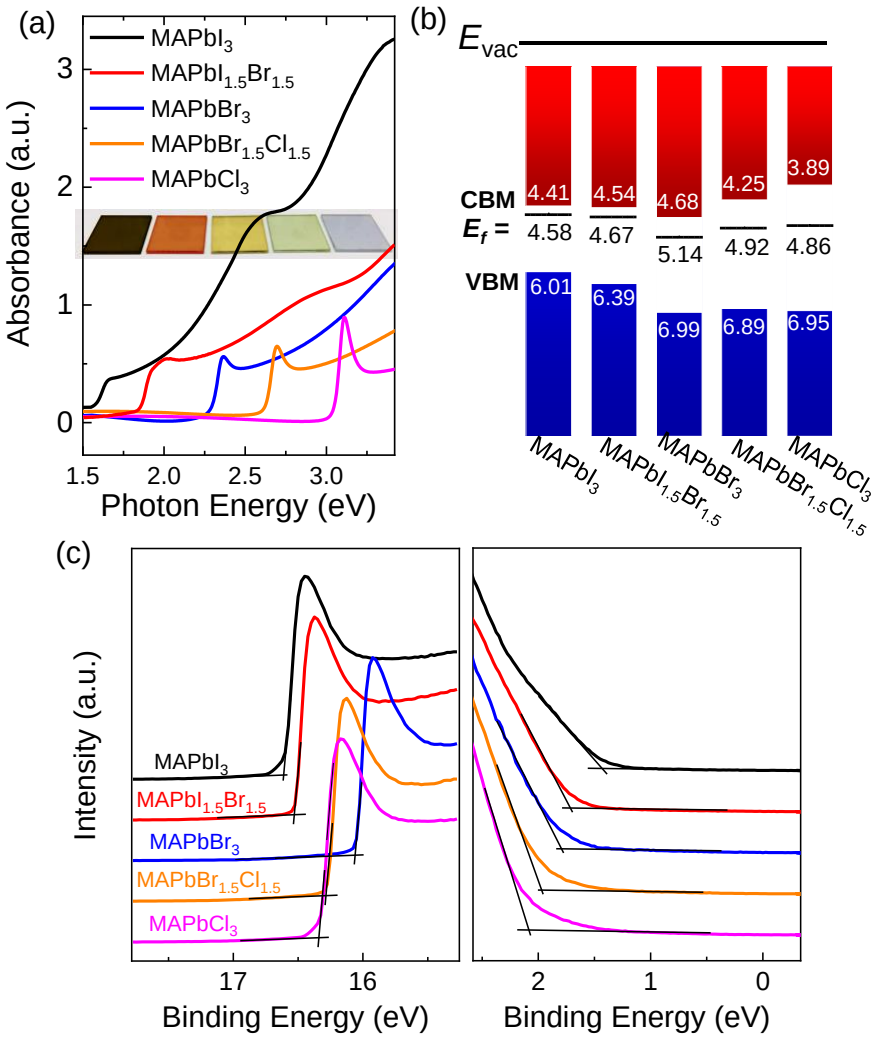

Figure 2. (a) UV-Vis absorption spectra of mixed-halide perovskite films. Insert: photographs of each perovskite thin film. (b) Schematics of the electronic structure of the mixed-halide perovskite films near the bandgap region. (c) UPS secondary electron edge (SEE) and the low binding energy region (near the Fermi energy E_F = 0 eV) of mixed-halide perovskite films. The onset of ionization of filled states relative to zero binding energy is used to track the shifts of E_F relative to VBM.

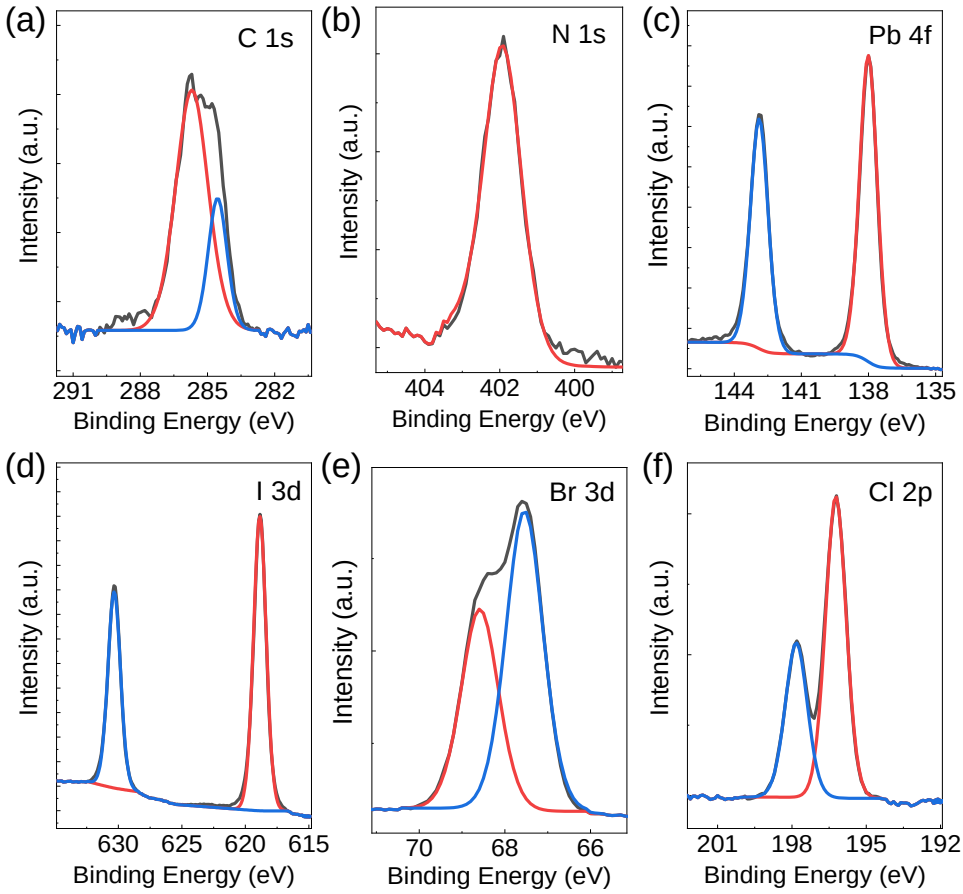

Figure 3. Representative XPS core-level spectra of (a) C 1s, (b) N 1s, (c) Pb 4f, and (d) I 3d in $MAPbI_3$, (e) Br 3d in $MAPbBr_3$, and (f) Cl 2p in $MAPbCl_3$ perovskite films.

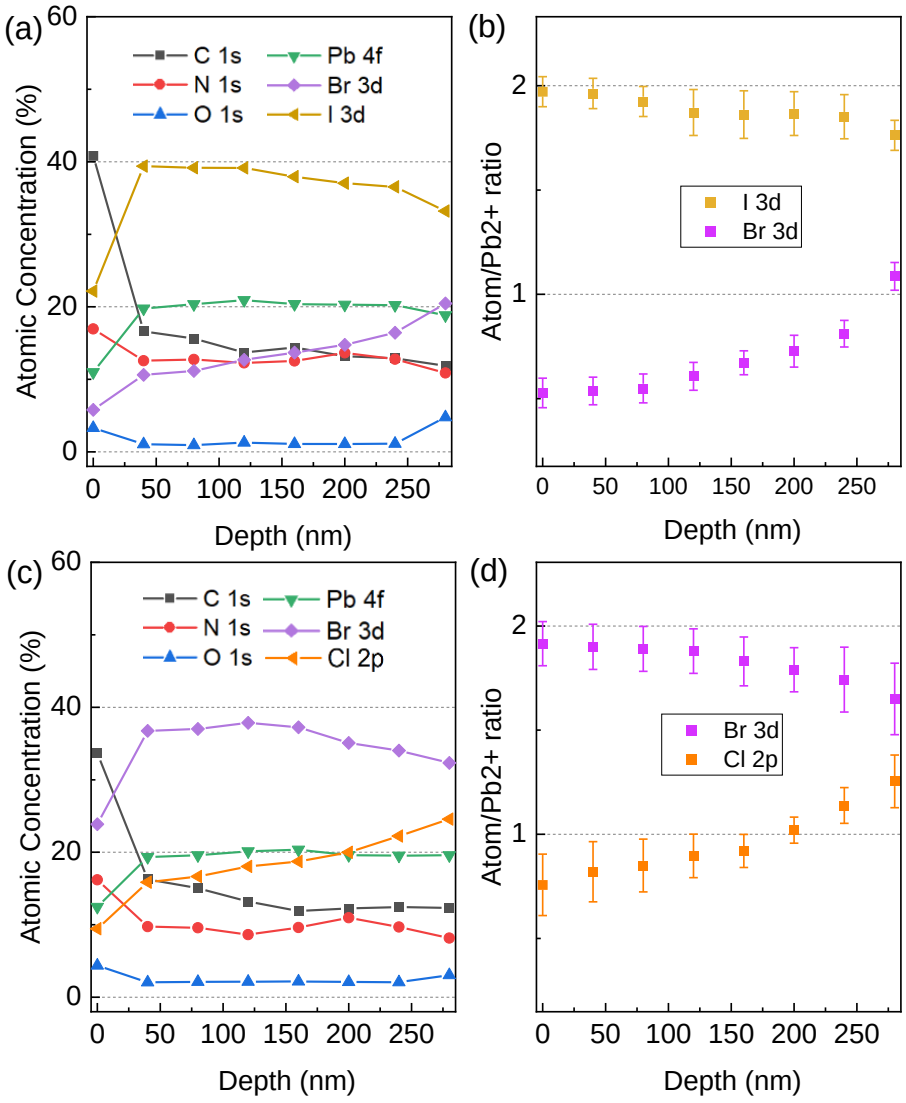

Figure 4. Representative XPS depth profile of (a) $MAPbI_{1.5}Br_{1.5}$ and (c) $MAPbBr_{1.5}Cl_{1.5}$ perovskite films. The atomic ratios of halides and metal cations relative to lead Pb^{2+} in (b) $MAPbI_{1.5}Br_{1.5}$ and (d) $MAPbBr_{1.5}Cl_{1.5}$. Error bars indicate the standard deviation from averaging the results obtained from different spots.

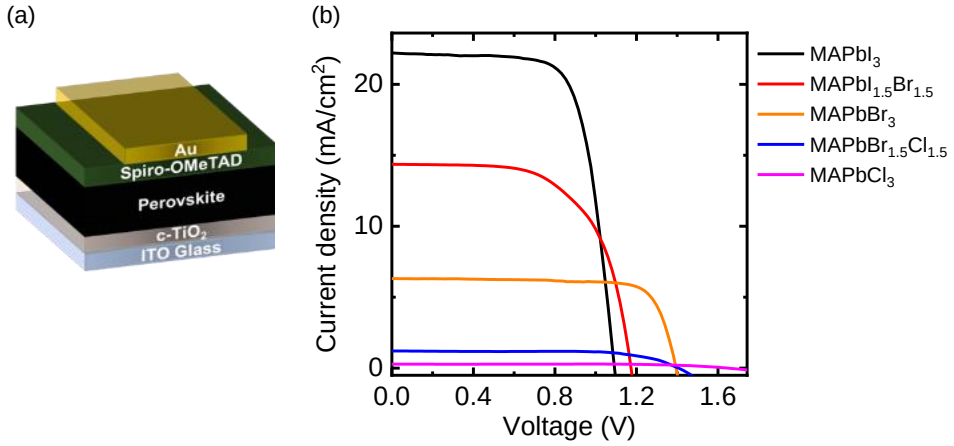

Figure 5. (a) The schematic diagram of the solar cell devices. (b) *J*–*V* curve for the peak efficiency for mixed-halide perovskite solar cells under AM1.5G illumination.

Table 1. PV parameters of classic $MAPbI_3$ and wide-bandgap $MAPbI_{3-x}Br_x$ and $MAPbBr_{3-x}Cl_x$ (x = 0 to 3) hybrid perovskite solar cells.

Perovskites		V_{OC} (V)	J_{SC} (mA/cm^2)	*FF* (%)	PCE (%)
$MAPbI_3$	Average	1.04 ± 0.03	21.88 ± 0.53	71.19 ± 2.51	16.25 ± 0.92
	Best	1.09	22.19	71.65	17.33
$MAPbI_{1.5}Br_{1.5}$	Average	1.15 ± 0.02	13.85 ± 0.60	68.30 ± 0.86	10.87 ± 0.69
	Best	1.19	14.60	69.40	12.06
$MAPbBr_3$	Average	1.38 ± 0.03	6.13 ± 0.15	76.97 ± 1.50	6.51 ± 0.26
	Best	1.40	6.31	78.30	6.92
$MAPbBr_{1.5}Cl_{1.5}$	Average	1.40 ± 0.01	1.13 ± 0.12	68.21 ± 4.91	1.08 ± 0.13
	Best	1.41	1.26	69.04	1.23
$MAPbCl_3$	Average	1.64 ± 0.03	0.26 ± 0.03	67.82 ± 2.66	0.29 ± 0.03
	Best	1.65	0.28	69.44	0.32

ASSOCIATED CONTENT

Supporting Information.

The Supporting Information is available free of charge on the ACS Publications website.

AUTHOR INFORMATION

Corresponding Author

*E-mail:siyuan.zhang@nist.gov (S.Z.).

*E-mail:christina.hacker@nist.gov (C.A.H.).

Author Contributions

S. Zhang and M.-C. Tang contributed equally to this work. S. Zhang, M.-C. Tang, T. D. Anthopoulos, and C. A. Hacker conceived and planned the experiments. S. Zhang performed the UPS and XPS measurements. M.-C. Tang prepared the samples and performed the UV-vis and SEM measurements, and performed solar cell fabrication and characterization. N. V. Nguyen measured and simulated the ellipsometry spectra. All authors provided critical feedback and helped shape the research, analysis, and manuscript.

Funding Sources

This work was supported by the National Institute of Standards and Technology (NIST) Financial Assistance Award with Federal Award ID 70NANB16H228, King Abdullah University of Science and Technology (KAUST), and National Natural Science Foundation of China (61974085).

REFERENCES

1. Laboratory, N. R. E. Best Research-Cell Efficiencies Chart. https://www.nrel.gov/pv/assets/pdfs/best-research-cell-efficiencies.20200104.pdf (accessed 01 April 2020).

2. Sutherland, B. R.; Sargent, E. H., Perovskite photonic sources. *Nat. Photonics* **2016,** *10* (5), 295.

3. Zhu, H.; Fu, Y.; Meng, F.; Wu, X.; Gong, Z.; Ding, Q.; Gustafsson, M. V.; Trinh, M. T.; Jin, S.; Zhu, X. J. N. m., Lead halide perovskite nanowire lasers with low lasing thresholds and high quality factors. *Nat. Mater.* **2015,** *14* (6), 636-642.

4. Dou, L.; Yang, Y. M.; You, J.; Hong, Z.; Chang, W.-H.; Li, G.; Yang, Y., Solution-processed hybrid perovskite photodetectors with high detectivity. *Nat. Commun.* **2014,** *5* (1), 1-6.

5. Balaz, S.; Porter, S. H.; Woodward, P. M.; Brillson, L. J., Electronic structure of tantalum oxynitride perovskite photocatalysts. *Chem. Mater.* **2013,** *25* (16), 3337-3343.

6. Lin, Y. H.; Pattanasattayavong, P.; Anthopoulos, T. D. J. A. M., Metal-Halide Perovskite Transistors for Printed Electronics: Challenges and Opportunities. *Adv. Mater.* **2017,** *29* (46), 1702838.

7. Yoo, E. J.; Lyu, M.; Yun, J. H.; Kang, C. J.; Choi, Y. J.; Wang, L. J. A. M., Resistive switching behavior in organic–inorganic hybrid CH3NH3PbI3− xClx perovskite for resistive random access memory devices. *Adv. Mater.* **2015,** *27* (40), 6170-6175.

8. Shah, A.; Torres, P.; Tscharner, R.; Wyrsch, N.; Keppner, H., Photovoltaic technology: the case for thin-film solar cells. *Science* **1999,** *285* (5428), 692-698.

9. Chang, Y.-C.; Liu, C.-H.; Liu, C.-H.; Zhang, S.; Marder, S. R.; Narimanov, E. E.; Zhong, Z.; Norris, T. B., Realization of mid-infrared graphene hyperbolic metamaterials. **2016,** *7*, 10568.

10. Anaya, M.; Lozano, G.; Calvo, M. E.; Míguez, H., ABX3 perovskites for tandem solar cells. *Joule* **2017,** *1* (4), 769-793.

11. Tan, H.; Jain, A.; Voznyy, O.; Lan, X.; Garcia de Arquer, F. P.; Fan, J. Z.; Quintero-Bermudez, R.; Yuan, M.; Zhang, B.; Zhao, Y.; Fan, F.; Li, P.; Quan, L. N.; Zhao, Y.; Lu, Z. H.; Yang, Z.; Hoogland, S.; Sargent, E. H., Efficient and stable solution-processed planar perovskite solar cells via contact passivation. *Science* **2017,** *355* (6326), 722-726.

12. Bi, D.; Yi, C.; Luo, J.; Décoppet, J.-D.; Zhang, F.; Zakeeruddin, Shaik M.; Li, X.; Hagfeldt, A.; Grätzel, M., Polymer-templated nucleation and crystal growth of perovskite films for solar cells with efficiency greater than 21%. *Nature Energy* **2016,** *1* (10), 16142.

13. Shin, S. S.; Yeom, E. J.; Yang, W. S.; Hur, S.; Kim, M. G.; Im, J.; Seo, J.; Noh, J. H.; Seok, S. I., Colloidally prepared La-doped BaSnO3 electrodes for efficient, photostable perovskite solar cells. *Science* **2017,** *356* (6334), 167-171.

14. Wu, Y.; Xie, F.; Chen, H.; Yang, X.; Su, H.; Cai, M.; Zhou, Z.; Noda, T.; Han, L., Thermally Stable MAPbI3 Perovskite Solar Cells with Efficiency of 19.19% and Area over 1 cm(2) achieved by Additive Engineering. *Adv. Mater.* **2017,** *29* (28), 1701073.

15. Chiang, C. H.; Nazeeruddin, M. K.; Gratzel, M.; Wu, C. G., The synergistic effect of H2O and DMF towards stable and 20% efficiency inverted perovskite solar cells. *Energy Environ. Sci.* **2017,** *10* (3), 808-817.

16. Tang, M.-C.; Zhang, S.; Magnanelli, T. J.; Nguyen, N. V.; Heilweil, E. J.; Anthopoulos, T. D.; Hacker, C. A., Unraveling the compositional heterogeneity and carrier dynamics of alkali cation doped 3D/2D perovskites with improved stability. *Mater. Adv.* **2021**.

17. Noh, J. H.; Im, S. H.; Heo, J. H.; Mandal, T. N.; Seok, S. I., Chemical management for colorful, efficient, and stable inorganic-organic hybrid nanostructured solar cells. *Nano Lett.* **2013,** *13* (4), 1764-9.

18. Maculan, G.; Sheikh, A. D.; Abdelhady, A. L.; Saidaminov, M. I.; Haque, M. A.; Murali, B.; Alarousu, E.; Mohammed, O. F.; Wu, T.; Bakr, O. M., CH3NH3PbCl3 Single Crystals: Inverse Temperature Crystallization and Visible-Blind UV-Photodetector. *J. Phys. Chem. Lett.* **2015,** *6* (19), 3781-6.

19. Heo, J. H.; Song, D. H.; Im, S. H., Planar CH3NH3PbBr3 hybrid solar cells with 10.4% power conversion efficiency, fabricated by controlled crystallization in the spin-coating process. *Adv. Mater.* **2014,** *26* (48), 8179-83.

20. Xu, J.; Boyd, C. C.; Zhengshan, J. Y.; Palmstrom, A. F.; Witter, D. J.; Larson, B. W.; France, R. M.; Werner, J.; Harvey, S. P.; Wolf, E. J., Triple-halide wide–band gap perovskites with suppressed phase segregation for efficient tandems. *Science* **2020,** *367* (6482), 1097-1104.

21. Hoke, E. T.; Slotcavage, D. J.; Dohner, E. R.; Bowring, A. R.; Karunadasa, H. I.; McGehee, M. D., Reversible photo-induced trap formation in mixed-halide hybrid perovskites for photovoltaics. *Chem. Sci.* **2015,** *6* (1), 613-617.

22. Elmelund, T.; Seger, B.; Kuno, M.; Kamat, P. V., How Interplay between Photo and Thermal Activation Dictates Halide Ion Segregation in Mixed Halide Perovskites. *ACS Energy Lett.* **2020,** *5* (1), 56-63.

23. Chen, W.; Mao, W.; Bach, U.; Jia, B.; Wen, X., Tracking Dynamic Phase Segregation in Mixed-Halide Perovskite Single Crystals under Two-Photon Scanning Laser Illumination. *Small Methods* **2019,** *3* (11), 1900273.

24. McMeekin, D. P.; Sadoughi, G.; Rehman, W.; Eperon, G. E.; Saliba, M.; Hörantner, M. T.; Haghighirad, A.; Sakai, N.; Korte, L.; Rech, B. J. S., A mixed-cation lead mixed-halide perovskite absorber for tandem solar cells. *Science* **2016,** *351* (6269), 151-155.

25. Bush, K. A.; Frohna, K.; Prasanna, R.; Beal, R. E.; Leijtens, T.; Swifter, S. A.; McGehee, M. D., Compositional engineering for efficient wide band gap perovskites with improved stability to photoinduced phase segregation. *ACS Energy Lett.* **2018,** *3* (2), 428-435.

26. Kubicki, D. J.; Prochowicz, D.; Hofstetter, A.; Zakeeruddin, S. M.; Grätzel, M.; Emsley, L., Phase Segregation in Cs-, Rb- and K-Doped Mixed-Cation (MA)x(FA)1–xPbI3 Hybrid Perovskites from Solid-State NMR. *J. Am. Chem. Soc.* **2017,** *139* (40), 14173-14180.

27. Luo, D.; Yang, W.; Wang, Z.; Sadhanala, A.; Hu, Q.; Su, R.; Shivanna, R.; Trindade, G. F.; Watts, J. F.; Xu, Z.; Liu, T.; Chen, K.; Ye, F.; Wu, P.; Zhao, L.; Wu, J.; Tu, Y.; Zhang, Y.; Yang, X.; Zhang, W.; Friend, R. H.; Gong, Q.; Snaith, H. J.; Zhu, R., Enhanced photovoltage for inverted planar heterojunction perovskite solar cells. *Science* **2018,** *360* (6396), 1442-1446.

28. Jeon, N. J.; Noh, J. H.; Kim, Y. C.; Yang, W. S.; Ryu, S.; Seok, S. I., Solvent engineering for high-performance inorganic–organic hybrid perovskite solar cells. *Nat. Mater.* **2014,** *13,* 897.

29. Wang, K.; Tang, M. C.; Dang, H. X.; Munir, R.; Barrit, D.; De Bastiani, M.; Aydin, E.; Smilgies, D. M.; De Wolf, S.; Amassian, A., Kinetic Stabilization of the Sol-Gel State in Perovskites Enables Facile Processing of High-Efficiency Solar Cells. *Adv. Mater.* **2019,** *31* (32), e1808357.

30. Lu, H.; Zhang, H.; Yuan, S.; Wang, J.; Zhan, Y.; Zheng, L., An optical dynamic study of MAPbBr3 single crystals passivated with MAPbCl3/I3-MAPbBr3 heterojunctions. *Phys Chem Chem Phys* **2017,** *19* (6), 4516-4521.

31. Liu, Y.; Yang, Z.; Cui, D.; Ren, X.; Sun, J.; Liu, X.; Zhang, J.; Wei, Q.; Fan, H.; Yu, F.; Zhang, X.; Zhao, C.; Liu, S. F., Two-Inch-Sized Perovskite CH3 NH3 PbX3 (X = Cl, Br, I) Crystals: Growth and Characterization. *Adv Mater* **2015,** *27* (35), 5176-83.

32. Knight, A. J.; Herz, L. M., Preventing phase segregation in mixed-halide perovskites: a perspective. *Energy Environ. Sci.* **2020,** *13* (7), 2024-2046.

33. Xie, L.-Q.; Chen, L.; Nan, Z.-A.; Lin, H.-X.; Wang, T.; Zhan, D.-P.; Yan, J.-W.; Mao, B.-W.; Tian, Z.-Q., Understanding the Cubic Phase Stabilization and Crystallization Kinetics in Mixed Cations and Halides Perovskite Single Crystals. *J. Am. Chem. Soc.* **2017,** *139* (9), 3320-3323.

34. Comin, R.; Walters, G.; Thibau, E. S.; Voznyy, O.; Lu, Z.-H.; Sargent, E. H., Structural, optical, and electronic studies of wide-bandgap lead halide perovskites. *J. Mater. Chem. C* **2015,** *3* (34), 8839-8843.

35. Noh, J. H.; Im, S. H.; Heo, J. H.; Mandal, T. N.; Seok, S. I., Chemical management for colorful, efficient, and stable inorganic–organic hybrid nanostructured solar cells. *Nano Lett.* **2013,** *13* (4), 1764-1769.

36. Li, D.; Cheng, H. C.; Wang, Y.; Zhao, Z.; Wang, G.; Wu, H.; He, Q.; Huang, Y.; Duan, X., The effect of thermal annealing on charge transport in organolead halide perovskite microplate field-effect transistors. *Adv. Mater.* **2017,** *29* (4), 1601959.

37. Canicoba, N. D.; Zagni, N.; Liu, F.; Mccuistian, G.; Fernando, K.; Bellezza, H.; Traore, B.; Rogel, R.; Tsai, H.; Le Brizoual, L., Halide Perovskite High-k Field Effect Transistors with Dynamically Reconfigurable Ambipolarity. *ACS Mater. Lett.* **2019,** *1* (6), 633-640.

38. Li, D.; Wang, G.; Cheng, H.-C.; Chen, C.-Y.; Wu, H.; Liu, Y.; Huang, Y.; Duan, X., Size-dependent phase transition in methylammonium lead iodide perovskite microplate crystals. *Nat. Commun.* **2016,** *7* (1), 1-8.

39. Frolova, L. A.; Dremova, N. N.; Troshin, P. A., The chemical origin of the p-type and n-type doping effects in the hybrid methylammonium–lead iodide (MAPbI3) perovskite solar cells. *Chem. Commun.* **2015,** *51* (80), 14917-14920.

40. Wang, Q.; Shao, Y.; Xie, H.; Lyu, L.; Liu, X.; Gao, Y.; Huang, J., Qualifying composition dependent p and n self-doping in CH3NH3PbI3. *Appl. Phys. Lett.* **2014,** *105* (16), 163508.

41. Li, C.; Wei, J.; Sato, M.; Koike, H.; Xie, Z.-Z.; Li, Y.-Q.; Kanai, K.; Kera, S.; Ueno, N.; Tang, J.-X., Halide-substituted electronic properties of organometal halide perovskite films: direct and inverse photoemission studies. *ACS Appl. Mater. Interfaces* **2016,** *8* (18), 11526-11531.

42. Xie, H.; Liu, X.; Lyu, L.; Niu, D.; Wang, Q.; Huang, J.; Gao, Y., Effects of precursor ratios and annealing on electronic structure and surface composition of CH3NH3PbI3 perovskite films. *J. Phys. Chem. C* **2015,** *120* (1), 215-220.

43. Liu, L.; McLeod, J. A.; Wang, R.; Shen, P.; Duhm, S., Tracking the formation of methylammonium lead triiodide perovskite. *Appl. Phys. Lett.* **2015,** *107* (6), 061904.

44. Busby, Y.; Noël, C.; Pescetelli, S.; Agresti, A.; Di Carlo, A.; Pireaux, J.-J.; Houssiau, L. In *XPS depth profiles of organo lead halide layers and full perovskite solar cells by variable-size*

argon clusters, Physical Chemistry of Semiconductor Materials and Interfaces XVII, International Society for Optics and Photonics: 2018; p 1072408.

45. Zhou, Y.; Wang, F.; Fang, H.-H.; Loi, M. A.; Xie, F.-Y.; Zhao, N.; Wong, C.-P., Distribution of bromine in mixed iodide–bromide organolead perovskites and its impact on photovoltaic performance. *J Mater. Chem. A* **2016,** *4* (41), 16191-16197.

46. Zhang, S.; Tang, M.-C.; Fan, Y.; Li, R.; Nguyen, N. V.; Zhao, K.; Anthopoulos, T. D.; Hacker, C. A., Role of Alkali-Metal Cations in Electronic Structure and Halide Segregation of Hybrid Perovskites. *ACS Appl. Mater. Interfaces* **2020,** *12* (30), 34402-34412.

47. Kuno, M.; Brennan, M. C., What Exactly Causes Light-Induced Halide Segregation in Mixed-Halide Perovskites? *Matter* **2020,** *2* (1), 21-23.

48. deQuilettes, D. W.; Zhang, W.; Burlakov, V. M.; Graham, D. J.; Leijtens, T.; Osherov, A.; Bulović, V.; Snaith, H. J.; Ginger, D. S.; Stranks, S. D., Photo-induced halide redistribution in organic–inorganic perovskite films. *Nat. Commun.* **2016,** *7* (1), 11683.

49. Stoumpos, C. C.; Malliakas, C. D.; Kanatzidis, M. G., Semiconducting Tin and Lead Iodide Perovskites with Organic Cations: Phase Transitions, High Mobilities, and Near-Infrared Photoluminescent Properties. *Inorg. Chem.* **2013,** *52* (15), 9019-9038.

50. Belisle, R. A.; Bush, K. A.; Bertoluzzi, L.; Gold-Parker, A.; Toney, M. F.; McGehee, M. D., Impact of Surfaces on Photoinduced Halide Segregation in Mixed-Halide Perovskites. *ACS Energy Lett.* **2018,** *3* (11), 2694-2700.

51. Akkerman, Q. A.; Bladt, E.; Petralanda, U.; Dang, Z.; Sartori, E.; Baranov, D.; Abdelhady, A. L.; Infante, I.; Bals, S.; Manna, L., Fully Inorganic Ruddlesden–Popper Double Cl–I and Triple Cl–Br–I Lead Halide Perovskite Nanocrystals. *Chem. Mater.* **2019,** *31* (6), 2182-2190.

52. Zheng, X. J.; Chen, B.; Yang, M. J.; Wu, C. C.; Orler, B.; Moore, R. B.; Zhu, K.; Priya, S., The Controlling Mechanism for Potential Loss in CH3NH3PbBr3 Hybrid Solar Cells. *ACS Energy Lett.* **2016,** *1* (2), 424-430.

53. Yao, H.; Ye, L.; Zhang, H.; Li, S.; Zhang, S.; Hou, J., Molecular Design of Benzodithiophene-Based Organic Photovoltaic Materials. *Chem. Rev.* **2016,** *116*, 7397-7457.

ToC figure

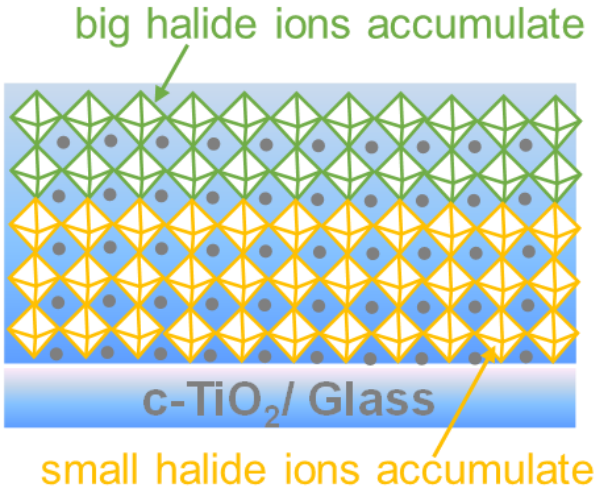
big halide ions accumulate
c-TiO2/ Glass
small halide ions accumulate

Supporting information

Wide Bandgap Mixed-halide 3D Perovskites: Electronic Structure and Halide Segregation Investigation

Siyuan Zhang,[†^*] *Ming-Chun Tang,*[†‖§] *Nhan V. Nguyen,*[†] *Thomas D. Anthopoulos,*[‖*] *Christina A. Hacker*[†*]

[†]Physical Measurement Laboratory, National Institute of Standards and Technology (NIST) Gaithersburg, MD 20899, USA

[‖]King Abdullah University of Science and Technology (KAUST), KAUST Solar Center (KSC), and Physical Science and Engineering Division (PSE), Thuwal, 23955-6900, Saudi Arabia.

[§]Institute for Research in Electronics and Applied Physics & Maryland NanoCenter, University of Maryland, College Park, MD 20742, USA

[^] Theiss Research, La Jolla, CA 92037, USA

S. Z. and M-C. T. contributed equally to this work.

Table S1 Summary of the band structure and energy levels for pure and mixed-halide $MAPbX_3$ perovskite thin films.

Film	**$MAPbI_3$**	**$MAPbI_{1.5}Br_{1.5}$**	**$MAPbBr_3$**	**$MAPbBr_{1.5}Cl_{1.5}$**	**$MAPbCl_3$**
Band gap (eV)	1.60 ± 0.01	1.85 ± 0.02	2.31 ± 0.02	2.64 ± 0.03	3.06 ± 0.01
E_f (eV)	4.58 ± 0.04	4.67 ± 0.03	5.14 ± 0.04	4.92 ± 0.03	4.86 ± 0.04
$VBM - E_f$ (eV)	1.43 ± 0.03	1.72 ± 0.02	1.85 ± 0.03	1.97 ± 0.02	2.09 ± 0.03
VBM (eV)	6.01 ± 0.05	6.39 ± 0.04	6.99 ± 0.05	6.89 ± 0.04	6.95 ± 0.05
CBM (eV)	4.41 ± 0.05	4.54 ± 0.05	4.68 ± 0.03	4.25 ± 0.04	3.89 ± 0.05

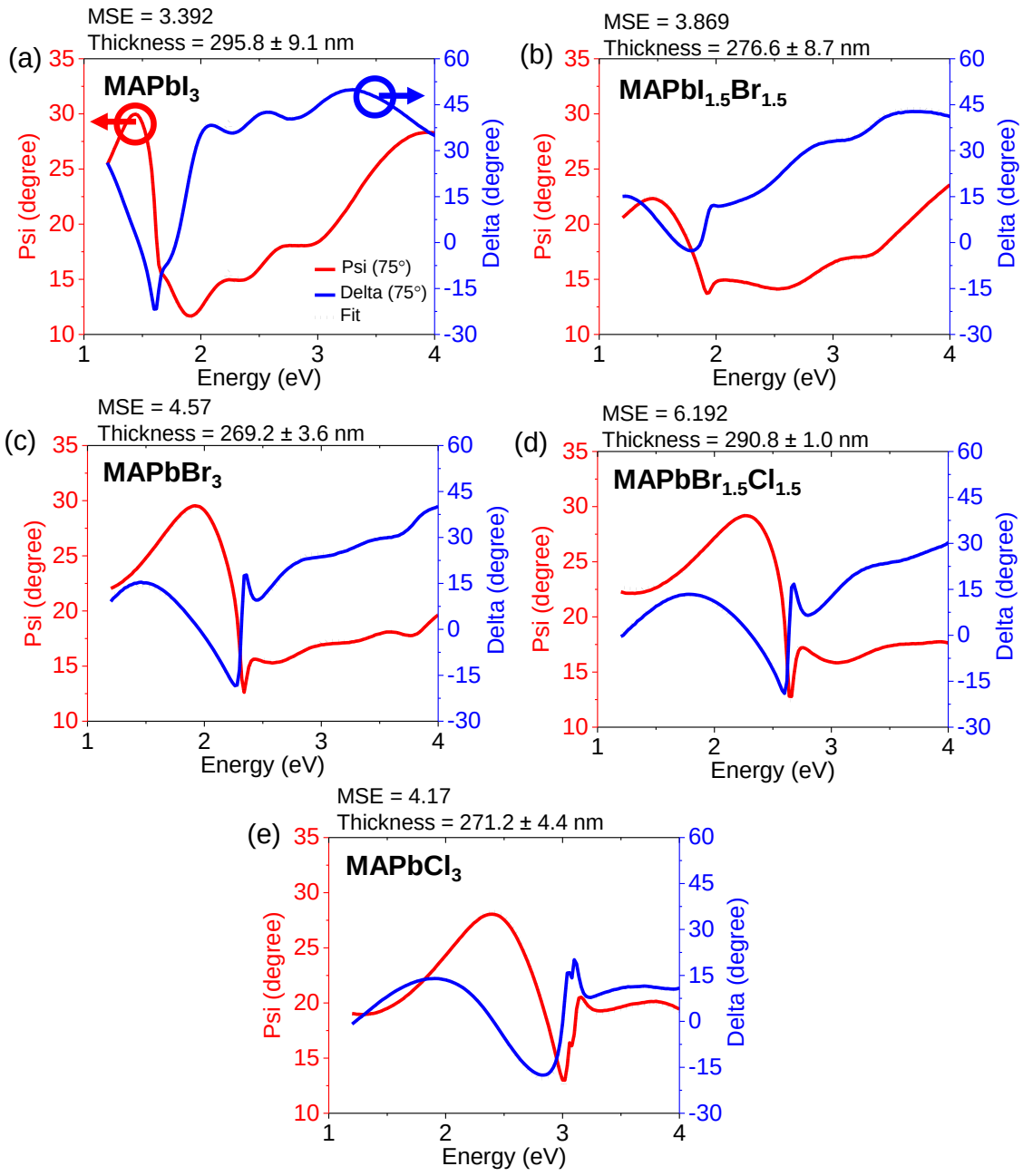

Figure S1. Measured and simulated ellipsometry spectra for mixed halide perovskite thin films: (a) $MAPbI_3$, (b) $MAPbI_{1.5}Br_{1.5}$, (c) $MAPbBr_3$, (d) $MAPbBr_{1.5}Cl_{1.5}$, and (e) $MAPbCl_3$ (MSE is mean square error).

Table S2. Summary of the thickness for mixed halide perovskite thin films measured by profiler and ellipsometry spectroscopy (SE).

Thickness (nm)	$MAPbI_3$	$MAPbI_{1.5}Br_{1.5}$	$MAPbBr_3$	$MAPbBr_{1.5}Cl_{1.5}$	$MAPbCl_3$
Profiler	295.8 ± 9.1	276.6 ± 8.7	269.2 ± 3.6	290.8 ± 1.0	271.2 ± 4.4
SE	310.5 ± 10.0	270.6 ± 11. 8	285.3 ± 5.7	300.8 ± 7.6	260. 3 ± 9.1

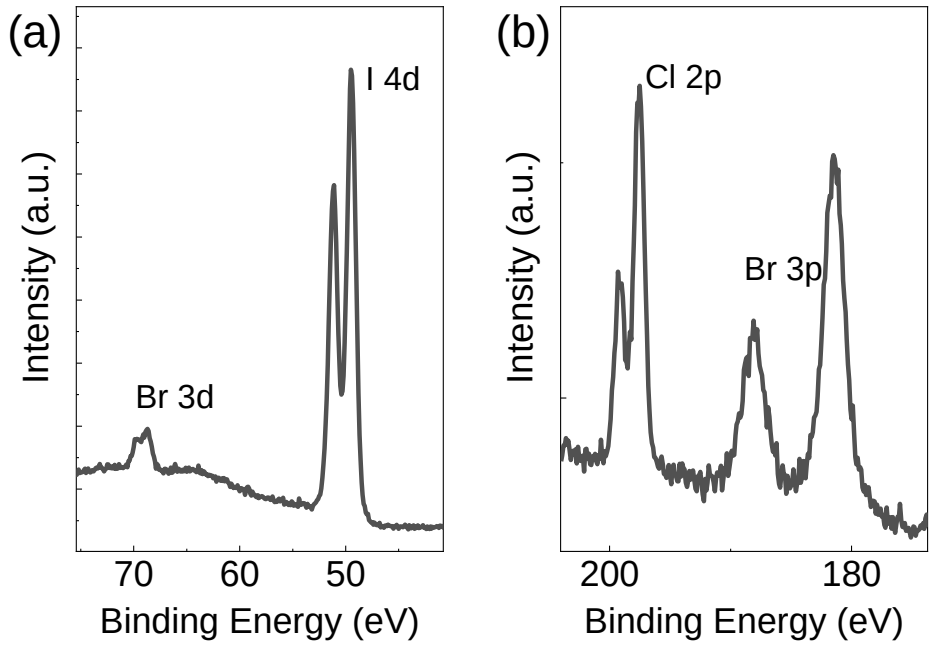

Figure S3. Representative XPS core-level spectra of (a) Br 3d and I 4d in $MAPbI_{1.5}Br_{1.5}$, (b) Cl 2p and Br 3p in $MAPbBr_{1.5}Cl_{1.5}$ perovskite films.

Table S3. PV parameters of classic $MAPbI_3$ and wide-bandgap $MAPbI_{3-x}Br_x$ and $MAPbBr_{3-x}Cl_x$ (x = 0 to 3) hybrid perovskite solar cells.

Perovskites		V_{OC} (V)	J_{SC} (mA/cm^2)	*FF* (%)	PCE (%)
$MAPbI_3$	Average	1.02 ± 0.04	21.47 ± 0.48	71.1 ± 0.67	17.20 ± 0.14
	Best	1.09	22.19	71.65	17.37
$MAPbI_{1.5}Br_{1.5}$	Average	1.15 ± 0.03	13.78 ± 0.51	68.56 ± 1.41	12.05 ± 0.30
	Best	1.19	14.54	69.40	12.41
$MAPbBr_3$	Average	1.38 ± 0.03	6.10 ± 0.14	77.00 ± 1.53	6.45 ± 0.23
	Best	1.40	6.31	78.30	6.90
$MAPbBr_{1.5}Cl_{1.5}$	Average	1.45 ± 0.04	1.13 ± 0.12	68.72 ± 5.22	1.09 ± 0.10

$MAPbCl_3$	Best	1.41	1.22	69.04	1.18
	Average	1.65 ± 0.02	0.29 ± 0.01	71.86 ± 4.97	0.26 ± 0.09
	Best	1.65	0.28	69.44	0.32